
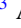




**Direct observation of skyrmions with arbitrary helicity in patterned Co/Pt multilayers**D. A. Tatarskiy <sup>1,2</sup>, N. S. Gusev,<sup>1</sup> Yu. V. Petrov,<sup>3</sup> A. Chuvilin <sup>4,5</sup>, M. V. Sapozhnikov <sup>1,2</sup> and S. A. Gusev <sup>1</sup><sup>1</sup>*Institute for Physics of Microstructures RAS, Nizhny Novgorod, GSP-105, Russia*<sup>2</sup>*Faculty of Physics, Lobachevsky State University, Nizhny Novgorod 603950, Russia*<sup>3</sup>*Department of Solid State Electronics, Saint-Petersburg State University, Saint-Petersburg 198504, Russia*<sup>4</sup>*CIC nanoGUNE BRTA, Donostia-San Sebastián E-20018, Spain*<sup>5</sup>*IKERBASQUE, Basque Foundation for Science, E-48009 Bilbao, Spain*

(Received 19 August 2023; revised 29 May 2024; accepted 11 July 2024; published 13 August 2024)

Co/Pt multilayers with perpendicular magnetic anisotropy were locally irradiated with a focused beam of He<sup>+</sup> ions to change the magnetic properties of the sample in strictly defined regions. Irradiated regions of 100–400-nm diameter served as pinning centers for chiral magnetic textures, resulting in the formation of magnetic skyrmions of the same diameter. The magnetization topology of such skyrmions was studied by Lorentz transmission electron microscopy. It was found that the helicity of skyrmions depended on its diameter and the ion irradiation fluence. Both Bloch-type skyrmions and Néel-type skyrmions, as well as skyrmions of the intermediate type, were observed. We assume that this behavior is due to a change in the balance of the magnetostatic energy and the Dzyaloshinskii-Moriya energy, which is confirmed by micromagnetic simulations.

DOI: [10.1103/PhysRevB.110.064415](https://doi.org/10.1103/PhysRevB.110.064415)**I. INTRODUCTION**

Soliton-like magnetization distributions (commonly referred to as “magnetic skyrmions”) in magnetic materials with easy-axis anisotropy have been known since the late 1970s [1–5]. Recently, they have demonstrated stability even at room temperature in thin multilayer films with heavy-metal (HM: Pt, Ir, W)–ferromagnet (FM: Fe, Co) interfaces [6–8]. The presence of heavy-metal layers in the magnetic films results in perpendicular magnetic anisotropy and the absence of inversion symmetry at the FM-HM interface. The latter leads to the existence of the interfacial-induced Dzyaloshinskii-Moriya (iDMI) exchange which stabilizes magnetic skyrmions. Because of this stability at room temperature, skyrmions are considered for possible application in spintronics devices [9,10].

Since the iDMI arises due to the lack of symmetry at the interface, its energy is equal to  $E = ([\mathbf{n} \times \mathbf{r}_{ij}] [\mathbf{S}_i \times \mathbf{S}_j])$ , where  $\mathbf{S}_{i,j}$  are the interacting magnetic moments,  $\mathbf{r}_{ij}$  is the radius vector between them, and  $\mathbf{n}$  is the normal to the interface. Due to this interaction, the magnetic moments line up in a cycloid rather than in a spiral, which is typical for a bulk DMI. This leads to the existence of domain walls and skyrmions of the Néel type in FM-HM multilayer films. In the last years many magnetic heterosystems have been experimentally investigated for hosting homochiral Néel domain walls and skyrmions at room temperatures: Fe/Ni/Cu [11], Pt/Co/AlO<sub>x</sub> [12], Pd/Co [13,14], Ta/Co/Pt [15,16], Ir/Co/Pt [17,18], Pt/Co/MgO [19], Fe/Ni/W [20], Ru/Co/W/Ru [21], and Pt/Co/W [22]. It should be remembered that in the absence of iDMI in the system, the Néel configuration has a higher magnetostatic energy than the Bloch configuration. The balance of magnetostatics and iDMI makes it possible to observe an intermediate state between the Bloch and Néel skyrmions—a canted (hybrid) skyrmion.

All these skyrmions are topologically identical, but differ in the direction of magnetization rotation, which is

characterized by such a parameter as helicity. While the helicity of the Bloch skyrmion is  $\gamma = \pm \pi/2$  and helicity of Néel skyrmions is  $\gamma = 0, \pi$  (depending on the iDMI sign), the helicity of the canted skyrmions takes intermediate values (Fig. 1).

The magnetostatic energy contribution can be “tuned” by varying the total film thickness [23–25]. The observation of canted domain walls (but not skyrmions) has been reported in several investigations [14,26].

Another way to control magnetic interactions in thin films is ion irradiation [27,28]. The irradiation causes a mixing of atoms at the FM/HM interfaces. This effect decreases the interfacial perpendicular anisotropy. Depending on the irradiation fluence, the perpendicular anisotropy can be reduced or even transformed into the in-plane one. The local decrease of the perpendicular anisotropy by irradiation of magnetic film by He<sup>+</sup> [29,30] or Ga<sup>+</sup> [31] ions allows to stabilize magnetic skyrmions even in the case of absent or weak iDMI. In this case the formation of Bloch-type magnetic skyrmions is observed [32].

We assumed that it is possible to change the ratio of the magnetostatic and iDMI energy of the skyrmion over a wide range by changing the radius of the locally irradiated region and the ion fluence. Here, we present the results of investigations of Co/Pt multilayers locally modified by fine focused beams of helium ions. The magnetic texture of the samples is studied using Lorentz transmission electron microscopy to reveal the conditions for the existence of Néel-, Bloch-, and intermediate-type skyrmions, which we call canted skyrmions.

**II. SAMPLES AND METHODS**

The specially designed nanostructured Co/Pt multilayered samples, which are the template for the formation of artificial

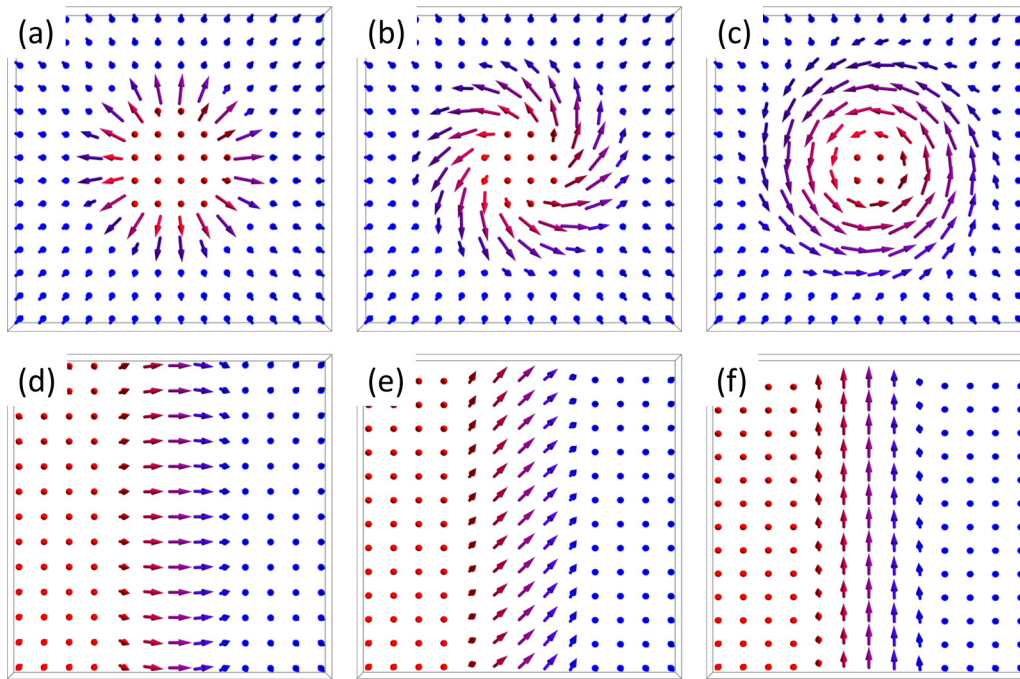


FIG. 1. Skyrmions (a)–(c) and domain walls (d)–(f) with different helicities  $\gamma = 0$  (Néel);  $\pi/4$  (canted);  $\pi/2$  (Bloch), correspondingly. The arrows show the direction of magnetization in the plane of the film; the colors indicate the perpendicular direction of magnetization (red is for up, blue is for down).

arrays of the magnetic skyrmions [29,33], are used in this work. The initial multilayers, consisting of five alternating Co (0.5 nm thick) and Pt (1 nm thick) layers are grown by dc magnetron sputtering on  $\text{Si}_3\text{N}_4$  silicon nitride amorphous membranes with a thickness of 30 and 50 nm with additional tantalum (10 nm) and platinum (10 nm) buffer layers. The deposition rates of the materials are 0.1 nm/s for cobalt and 0.3 nm/s for platinum. The thicknesses of the films are determined by the deposition time after preliminary calibration of the thicknesses of individual layers, measured by x-ray reflectometry. The film is covered with 2-nm-capping platinum layer to prevent oxidation.

Transmission electron microscopy (TEM) is performed on a LIBRA200 MC (Carl Zeiss) at 200 kV to study the film microstructure. We study the cross-sectional structure of multilayer films and analyze in-plane micrographs (Fig. 2). TEM lamella preparation is performed by cross-beam station Auriga Laser (Carl Zeiss). The fabricated cross sections are also polished using a low-energy ( $\sim 300$ -eV)  $\text{Ar}^+$  source to reduce the thickness of the damaged layers.

The high-resolution TEM image of the Co/Pt cross section [Fig. 2(a)] clearly shows the crystal lattice of cobalt and platinum layers with an interplanar spacing of 0.218 nm, which can correspond best to the (111) plane of the CoPt solid solution with  $Fm\bar{3}m$  space-group lattice symmetry. The average value of the Co layer thickness is 0.5 nm, and the thickness of the Pt layer is 1.0 nm, which are in good agreement with the values that were set by the time of the magnetron deposition of films. Analysis of TEM in-plane images of the film provides additional information on the microstructure of the Co/Pt sample. The selected area diffraction patterns of a film correspond to a cubic lattice [Fig. 2(c)] with lattice parameter  $a = 0.379 \pm 0.002$  nm and weak axial (111) texture. This value

is between the parameters of platinum lattice  $a_{\text{Pt}} = 0.392$  nm and cubic cobalt lattice  $a_{\text{Co}} = 0.354$  nm. A typical dark-field micrograph of Co/Pt polycrystalline multilayer is shown in Fig. 2(b). The full width at half maximum of autocorrelation function is  $\sim 5.6$  nm. This value can be taken for calculation of volume-weighted average grain size [34,35] and is used in the micromagnetic simulations.

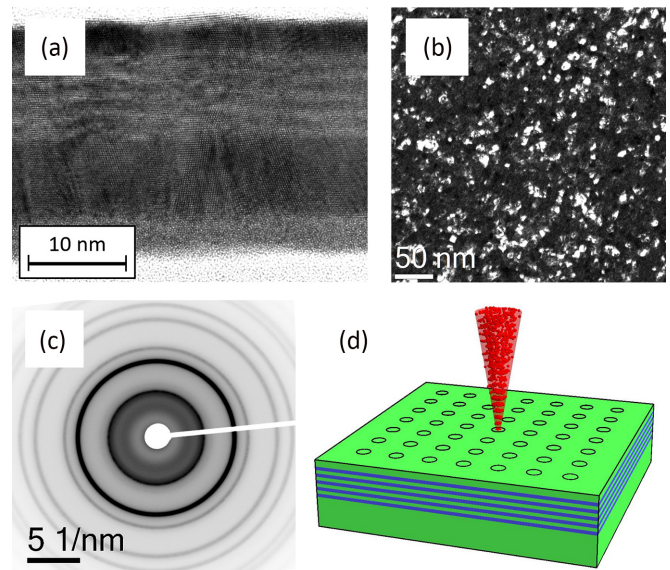


FIG. 2. (a) High-resolution cross-section micrograph of multilayer; the distance between atomic planes is  $\sim 0.218$  nm; (b) The dark-field plane-view micrograph of Co/Pt multilayer. (c) Selected area diffraction pattern of planar specimen. (d) The geometry of nanomodification: the array of irradiated spots with the reduced anisotropy.

To reduce the interfacial perpendicular anisotropy in the samples locally, nanostructuring of multilayers is performed by irradiation with a focused He<sup>+</sup> beam. He<sup>+</sup> ion irradiation can change the iDMI as the latter has interfacial nature [36–38]. As a result the nanospots with the reduced anisotropy (we will refer them later simply as “spots” to be short) in the laterally uniform magnetic Co/Pt films are fabricated [Fig. 2(d)]. The irradiation procedure is carried out using the ORION (Carl Zeiss) helium ion microscope. We irradiated several arrays of spots of different diameters: 100, 200, and 400 nm. The fluences range from  $1.0 \times 10^{15}$  to  $8.0 \times 10^{15}$  ions per cm<sup>2</sup> and the energy of the ions was 30 keV. Fifteen regions were formed on every specimen: arrays of spots with different fluences and different diameters.

Such spots serve as pinning centers for magnetic skyrmions [39], and one can initialize them by the magnetization reversal of the sample [29].

Magnetization hysteresis loops of the Co/Pt films were studied by magneto-optical Kerr effect (MOKE) measurements using a custom-made magneto-optical stand with stabilized He-Ne laser ( $\lambda = 632$  nm). Lorentz TEM (L-TEM) measurements were performed at a C<sub>s</sub>-corrected TITAN 60–300 transmission electron microscope (FEI Company) operated at 80 kV utilizing the aberration-corrected Lorentz mode. In the Fresnel method the resulting magnetic image contrast depends on the defocus value and is proportional to the Z component of magnetization rotor. In our experiments, it is possible to observe in situ changes in the Fresnel contrast caused by an external magnetic field. The field is created at the location of the sample by weak excitation of the microscope objective lens and tilting the sample for the magnetization reversal. The maximum value of this magnetic field in our experiments was 35 mT along normal to the film.

Besides, such sophisticated nanostructuring gives us a possibility to manipulate the size of magnetic skyrmion, which is determined by the spot diameter. In order to verify experimentally observed transition of confined skyrmion states we carry out micromagnetic simulations. The simulation is performed utilizing graphics processing unit-accelerated MUMAX3 package [40] based on a numerical solution of the Landau-Lifshitz-Gilbert system of equations for the magnetization of the system

$$\partial \mathbf{M} / \partial t = -\gamma [\mathbf{M} \times \mathbf{H}_{\text{eff}}] - \gamma \alpha / M_s [\mathbf{M} \times [\mathbf{M} \times \mathbf{H}_{\text{eff}}]],$$

where  $\mathbf{M}$  is the magnetization,  $\gamma$  is the gyromagnetic ratio,  $\alpha$  is the dimensionless damping parameter, and  $M_s$  is the magnetization at saturation. The effective field  $\mathbf{H}_{\text{eff}} = -\delta E / \delta \mathbf{M}$  is a variation derivative of the free-energy functional. The total energy of the particle can be defined by

$$E = E_h + E_{\text{ex}} + E_A + E_m + E_D.$$

Here,  $E_h$  is the Zeeman energy of the magnetization interaction with an external magnetic field  $H$ .  $E_{\text{ex}}$  is the energy of the exchange interaction,  $E_A$  is energy of the interfacial uniaxial magnetic anisotropy,  $E_m$  is the magnetostatic energy, and  $E_D$  is interfacial DMI energy. Expressions for these terms have conventional form. Polycrystalline structure of the sample is simulated in MUMAX3 by the Voronoi tessellation method [41]. We suppose that each grain has its own value and direction of uniaxial volume anisotropy and iDMI strength.

Additionally, the film as a whole has an average nonzero perpendicular anisotropy caused by Co/Pt interface. For the sake of simplicity we use a model of random uniaxial anisotropy in each crystalline grain even if the crystallographic structure is cubic or hexagonal as for typical cobalt, platinum, and their alloys. Other material parameters of the CoPt multilayers used in the simulations are taken from our previous works and describe hysteresis loops with a good accuracy [32,42]. The appropriate value for average uniaxial anisotropy of the *as-deposited* film is  $K_u = 3.1 \times 10^4$  J/m<sup>3</sup>. This value stands for quality factor  $Q = K_u / (\mu_0 M_s^2 / 2) = 1.23$ . The exchange stiffness is  $J = 7 \times 10^{-13}$  J/m. The saturation magnetization is assumed to be 200 kA/m in the material. The parameters of modified spots are chosen by the best fit of MOKE and L-TEM data.

We simulated up to a  $1024 \times 1024 \times 7.5$ -nm<sup>3</sup> part of the film with a  $0.5 \times 0.5 \times 7.5$ -nm<sup>3</sup> unit cell. A total count of crystallites was around 1800 with different material parameters (variations of magnetic anisotropy value and its direction, iDMI value, etc.) This approach demonstrated a good approximation of a real random polycrystalline film. The iDMI and the volume anisotropy value for each crystallite were set randomly, and the maximum deviation did not exceed 15% from the average values.

The distributions of magnetization in the structures obtained by numerical calculations are used to simulate images with magnetic contrast in the transmission electron microscope. To simulate L-TEM images, a specially developed original PYTHON script for the GATAN MICROSCOPY SUITE SOFTWARE® is used [43]. It is known that the value of the contrast  $\Delta I$  in Fresnel mode is proportional to the projection of magnetization curl on the optical axis  $\mathbf{n}$  of an electron microscope and defocus value [44,45]:

$$\Delta I(\rho) \sim (\mathbf{n}[\nabla \times \mathbf{M}(\mathbf{r})]),$$

where  $\rho$  is a vector in the detector plane and  $\mathbf{r}$  is a vector in the plane of the film. In the general case, the sample is tilted, and the planes of the film and the detector do not coincide.

Néel and Bloch skyrmions [Figs. 3(a) and (g)] can be easily distinguished by comparing the contrast on Fresnel images. The simplest type of contrast is the contrast from pure Néel skyrmion. It is zero at zero tilt [Fig. 3(b)]. At nonzero tilt-angle Néel skyrmion shows dipolar black and white dot aligned with the tilting axis. This contrast appears due to the antiparallel orientation of magnetic moments in the central part of skyrmion and surrounding film. Typical Fresnel contrast of the tilted Néel skyrmion is presented in Fig. 3(c).

If the magnetization inside the irradiated spot curls into a vortex, then two magnetic configurations are possible. In the first case, the direction of the vortex core coincides with the direction of the magnetization in the surrounding film. Such a magnetization distribution, which we call the codirectional vortex (see Fig. 3 in Ref. [39]), is topologically trivial. On the contrary, if the magnetizations in the core and in the surrounding film are opposite, then such a state is topologically charged and is obviously a Bloch skyrmion. At the zero tilt, the contrast does not depend on the core direction but depends on the clockwise or counterclockwise swirl of magnetization, which produces focusing/defocusing effect on electron beam. So, a trivial codirectional vortex and Bloch skyrmion cannot

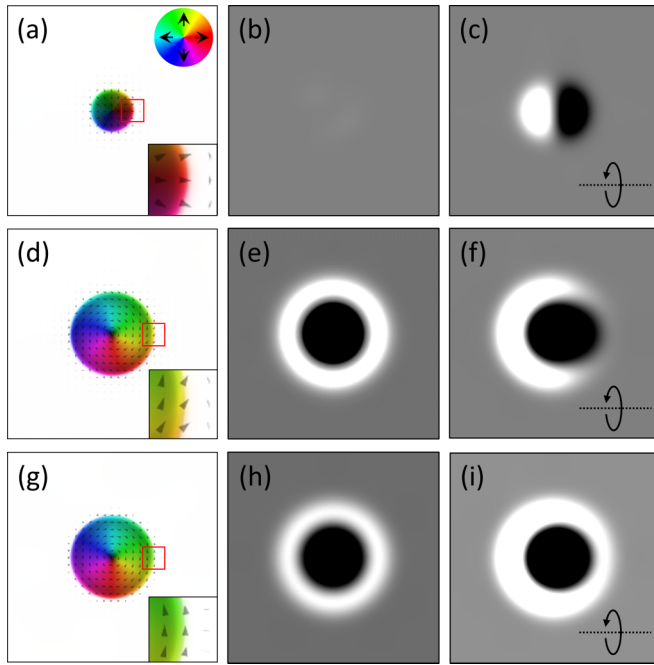


FIG. 3. Simulated magnetization distribution (left column), simulated Fresnel contrast without tilt (column in the center), and simulated Fresnel contrast at 30° tilt along vertical axis (right column) for the Néel skyrmion (first row), for the canted skyrmion (second row), and for the Bloch skyrmion (bottom row). In the insets of (d) and (g) the enlarged red areas are shown to highlight difference between canted and Bloch skyrmions.

be distinguished at the zero tilt. The situation changes with the tilt. At the tilt the contrast of the Bloch skyrmion is a sum of focusing/defocusing and dipolar contrast because of antiparallel orientation of the core part. Trivial codirectional vortex does not have such dipolar contribution in contrast. This way they can be distinguished in L-TEM observations. [Fig 5(b)].

### III. RESULTS AND DISCUSSION

The simulated magnetization curve and domain structures of the as-prepared film are represented in Figs. 4(a), 4(e), and 4(f), correspondingly. In both cases the micromagnetic simulations demonstrate a good quantitative agreement with experimental observations [compare Figs. 4(c) and 4(d) and Figs. 4(g) and 4(h)]. The initial film demonstrates the rectangular hysteresis loop which is typical for magnetic film with perpendicular easy-axis anisotropy [Fig. 4(a)]. In the demagnetized state the films exhibit a labyrinth domain structure. The experimental Fresnel micrographs of the observed domains corresponding to the different parts of the magnetization loops are presented in Figs. 4(b)–4(d). Although iDMI is characteristic of Co/Pt multilayers [46,47], the observation of labyrinth domains in the original unirradiated film indicates that the existence of iDMI alone is not sufficient for mass skyrmion formation.

Experimental observations confirm the presence of a nonzero iDMI in the studied films. The indication for iDMI is the existence of striped-type contrast on L-TEM images with

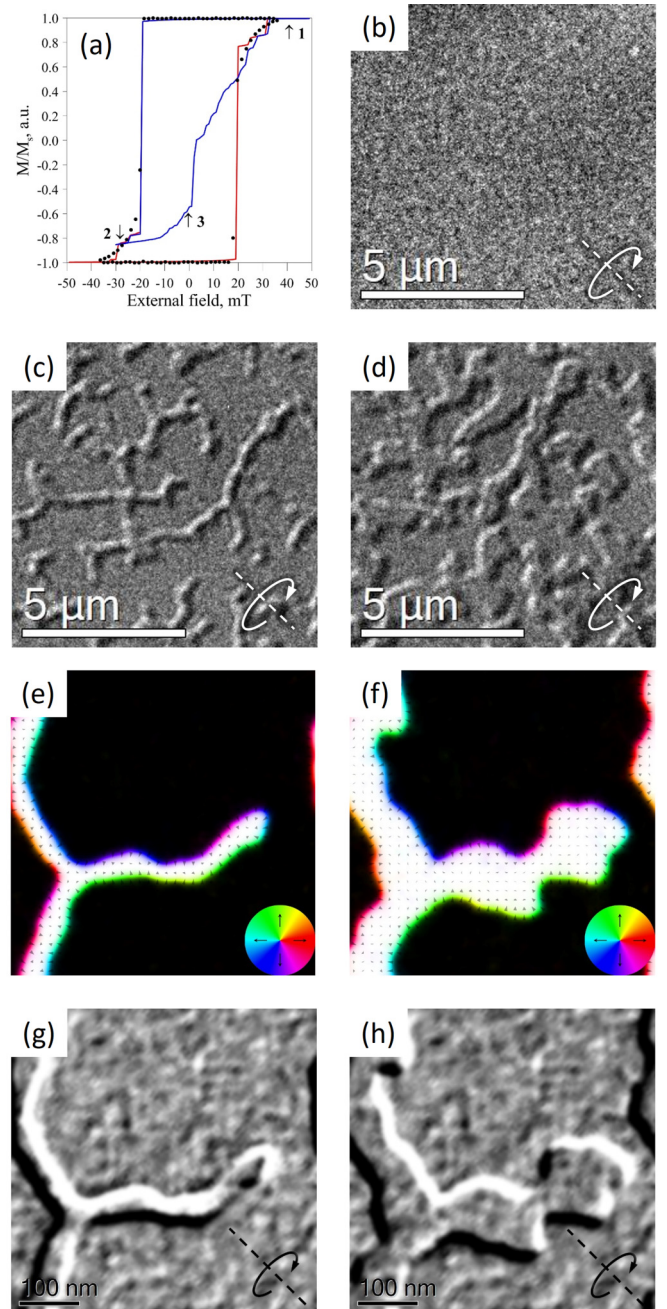


FIG. 4. (a) Polar MOKE major and minor hysteresis loops of the initial Co/Pt film with easy-axis perpendicular anisotropy. Circles: magneto-optical measurements; red curve: simulated hysteresis loop; blue curve: minor hysteresis loop; numbers indicate the points where the Fresnel contrast is acquired through *in situ* magnetization reversal. (b)–(d) Fresnel contrast on micrographs. Figures are acquired at points 1, 2, and 3 of the hysteresis curve, correspondingly. The contrasts are obtained at 30° tilt along denoted axis. (e), (f) Simulated magnetization distributions of points 2 and 3 from hysteresis curve, direction denoted by color wheel; black-white colors denote  $M_z$  direction. (g), (h) Simulated Fresnel contrast at 30° tilt along denoted axis.

the Fresnel contrast [Fig. 4(c)] in a certain range of external fields (excitations of the objective lens).

One can see the iDMI value is strong enough that domains walls have Néel structure. But, this value is small

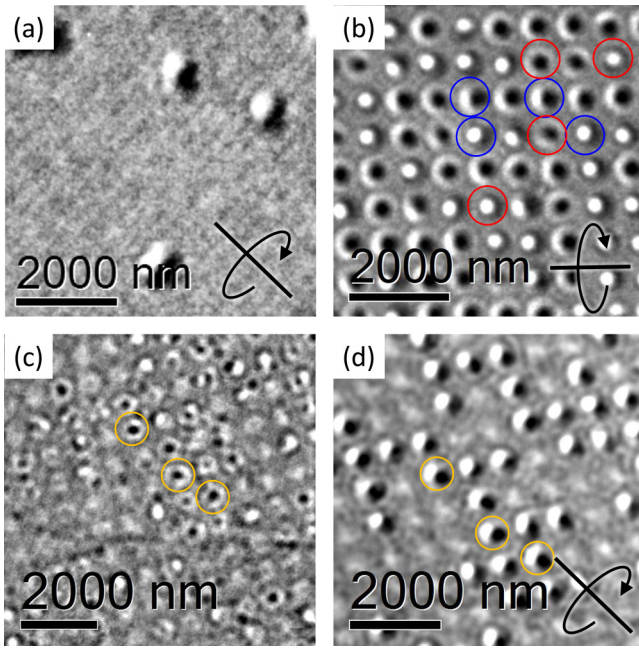


FIG. 5. (a) Typical Fresnel contrast of Néel skyrmions, obtained for the sample with array of the spot with diameter 200 nm, fluence  $2.0 \times 10^{15}$  ions per  $\text{cm}^2$ , tilt  $30^\circ$ ; compare Fig. 3(c). (b) Typical Fresnel contrast of Bloch skyrmions (marked by blue circles) and trivial codirectional vortex (marked by red circles). Obtained for the spots with 400-nm diameter, fluence  $3.0 \times 10^{15}$  ions per  $\text{cm}^2$ , tilt  $30^\circ$ ; compare Fig. 3(i). (c), (d) Fresnel contrast of canted skyrmions, obtained for the sample with array of the spot with diameter 400 nm and fluence  $2.0 \times 10^{15}$  ions per  $\text{cm}^2$ . Tilting angles  $0^\circ$  and  $30^\circ$ , correspondingly; compare Figs. 3(e) and 3(f). Same skyrmions on (c) and (d) are marked by yellow circles.

to stabilize isolated skyrmions. It is known that skyrmions are thermodynamically stable in case of iDMI stronger than  $D_{\text{sk}} = \sqrt{J(K_u + \mu_0 M_s^2/2)}/\pi$  [48], which is  $63.1 \mu\text{J}/\text{m}^2$  with material parameters of our samples. In the case of the initial unpatterned film we observed labyrinth domains with Néel domain walls. For our magnetic parameters the DMI value for Néel domain-wall formation should be higher than  $|D_{\text{cr}}| = 0.44\mu_0 M_s^2 t/\pi = 52.8 \mu\text{J}/\text{m}^2$ , where  $t = 7.5 \text{ nm}$  is the film thickness,  $\mu_0$  is vacuum permittivity and  $M_s = 200 \text{ kA}/\text{m}$  is saturation magnetization. So, the iDMI value in our case is somewhere between 53 and  $63 \mu\text{J}/\text{m}^2$ . For larger values of iDMI interaction, the formation of isolated skyrmions should be observed in the magnetic fields close to saturation, which we do not observe in our initial films. This allows us to estimate the upper possible value of the iDMI constant in nonirradiated areas of the samples. Further, we will use this estimated value in numeral calculations.

The behavior of the irradiated samples is quite different in the comparison with the initial film. They demonstrate the formation of different localized magnetic states within irradiated spots. Depending on the spot diameter and fluence we observe the formation of Néel and Bloch skyrmions, multivortices, or localized in-plane domains. These states can be easily identified on experimentally obtained L-TEM images (Fig. 5) by comparison with simulated Fresnel contrast (Fig. 3). Additional Fresnel contrast simulations with addition of material

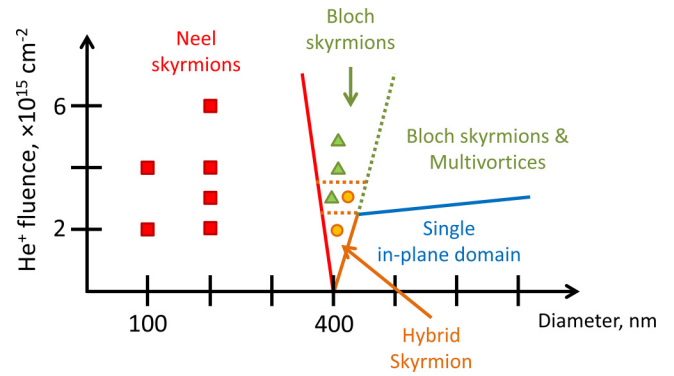


FIG. 6. Diagram of the stability of localized magnetic states. The experimentally observed states are marked by geometrical figures. The boundary lines are schematically drawn for ease of perception.

contrast for clockwise and counterclockwise skyrmions can be found in Supplemental Material (S1) [49]. Comparison of Bloch skyrmion and trivial codirectional vortex is also found in Supplemental Material (S2).

The experimental phase diagram of stability of magnetization states is presented in Fig. 6.

Besides the well-known Bloch and Néel skyrmions listed above we observe formation of the canted skyrmions with intermediate helicity. They demonstrate “Bloch”-type contrast at zero tilt and “dipolar” contrast at tilting [Figs. 5(c) and 5(d); compare with Figs. 3(d)–3(f)]. Canted skyrmions are stable only in the narrow window of spot diameter 400 nm and fluence  $2.0 \times 10^{15}$  ions per  $\text{cm}^2$ . We conclude that under these special conditions, the iDMI interaction and the magnetostatic interaction are comparable in magnitude, which leads to the stabilization of canted skyrmions. The interesting fact is that in smaller irradiated areas only the dipolar contrast exists, indicating that the iDMI energy prevails in this case. Thus, the stable type of the skyrmion depends not only on the fluence but on diameter of the modified area too.

The magnetostatic interaction is long range, while the iDMI is the antisymmetric exchange interaction with the nearest neighbors. In addition, in our system iDMI constant is weak enough, so the size of the skyrmion is determined by the size of the irradiated area in which it is pinned. Accordingly, as the skyrmion size increases, the magnetostatic energy begins to predominate, which leads to the transformation of the Néel skyrmion into the Bloch skyrmion. The magnetostatic energy also depends on the radiation dose due to the reduction in saturation magnetization. Thus, the canted skyrmions can be observed in the narrow range of ion fluences. At intermediate sizes, a balance between the magnetostatic energy and iDMI is possible, which leads to the formation of a skyrmion with an intermediate helicity.

We also carried out the micromagnetic simulations for the nanopatterned film. We use the introduced above material parameters for the as-deposited part of the film. In the radiated spots the used parameters are changed, namely, the uniaxial anisotropy constant  $K_u$  was varied in the range  $0.9 - 1.3 \times 10^4 \text{ J}/\text{m}^3$  ( $Q = 0.64 - 0.92$ ). We expect the fluence and  $K_u$  ( $Q$ ) have monotonic dependence. The saturation magnetization in

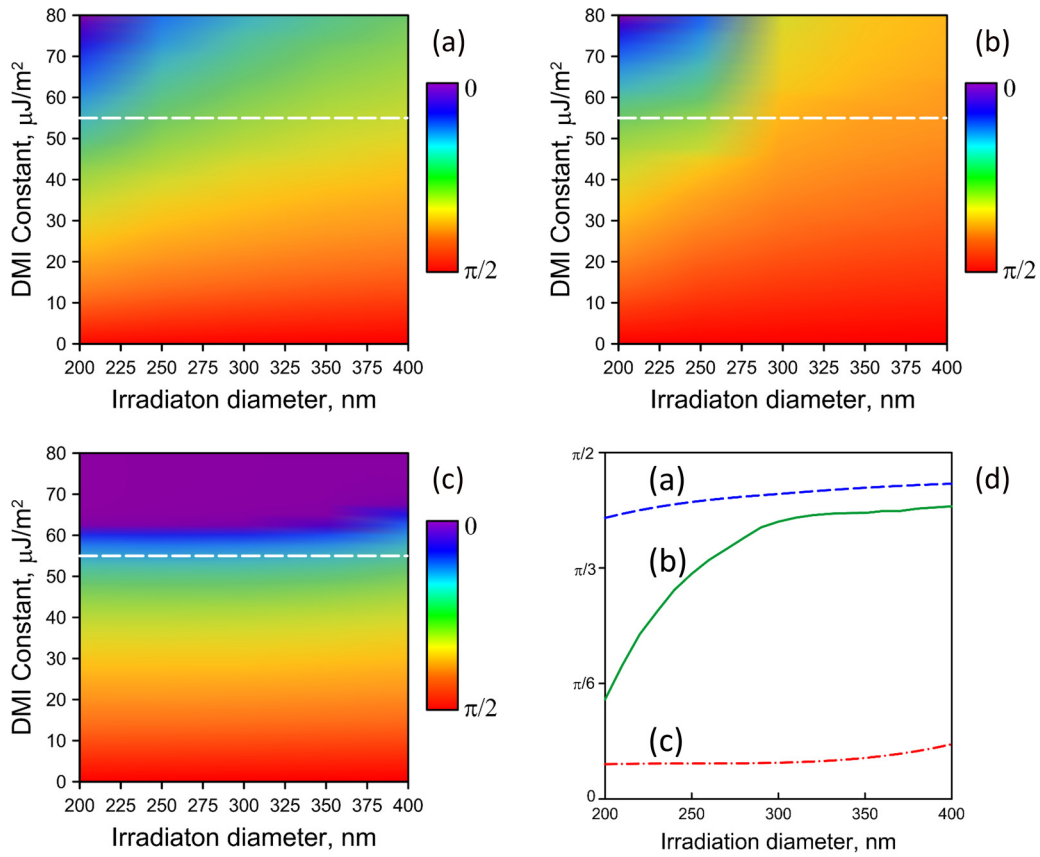


FIG. 7. Phase diagrams of skyrmion helicity vs diameter and DMI constant for different quality factor 0.64 (a), 0.78 (b), and 0.92 (c). Violet for pure Néel skyrmion, red for Bloch skyrmion. (d) Cross section of (a)–(c) at  $D = 55 \mu\text{J}/\text{m}^2$ ; green (solid) line:  $K_u = 1.1 \times 10^4 \text{ J}/\text{m}^3$ ; blue (dashed):  $K_u = 0.9 \times 10^4 \text{ J}/\text{m}^3$ ; red (dashed-dotted);  $K_u = 1.3 \times 10^4 \text{ J}/\text{m}^3$ .

the radiated spot is 150 kA/m; the iDMI strength in radiated area is taken as zero.

The calculated diagram of skyrmion helicity is presented in Figs. 7(a)–7(c) for different  $K_u$  ( $Q$ ). It demonstrates helicity of skyrmion states in nanomodified spot versus their diameters and iDMI strength. The helicity is calculated as an average angle between radial vector and in-plane component of magnetization. Zero angle stands for Néel skyrmion and  $\pi/2$  angle stands for Bloch skyrmion. As it can be seen from the phase diagrams the skyrmion helicities have weak dependence on irradiation diameter in case of high or low  $K_u$  ( $Q$ ) values [Figs. 7(a) and 7(c)]. The cross section of skyrmion helicity at iDMI  $D = 55 \mu\text{J}/\text{m}^2$  are given in Fig. 7(d). Thus, we assume that  $K_u = 1.1 \times 10^4 \text{ J}/\text{m}^3$  ( $Q = 0.78$ ) is typical for  $\text{He}^+$  fluence  $2.0 \times 10^{15}$  ions per  $\text{cm}^2$ .

#### IV. CONCLUSIONS

We have investigated Co/Pt multilayers both unpatterned and patterned by the focused  $\text{He}^+$  ion beam using the Lorentz transmission electron microscopy. The unpatterned films demonstrate the formation of  $360^\circ$  domain walls which confirms the existence of the iDMI in the film, although its value is insufficient for the formation of isolated skyrmions. On the contrary, the patterned films demonstrate the formation of different types of skyrmions: Bloch, Néel, and canted. The

spot with the reduced anisotropy plays a role of the local potential well for the skyrmion. Its helicity is determined by the balance of magnetostatic energy and DMI and depends on the size of the spot.

#### ACKNOWLEDGMENTS

This work was supported by the Center of Excellence “Center of Photonics” funded by the Ministry of Science and Higher Education of the Russian Federation, Contract No. 075–15–2022–316, and by the Spanish MICINN under the Maria de Maeztu Units of Excellence Program (Grants No. MDM-2016–0618 and No. CEX2020–001038-M). The equipment of the Interdisciplinary Resource Center under the direction of Nanotechnology (St. Petersburg State University) and facilities of Center “Physics and technology of micro- and nanostructures” (Institute for Physics of Microstructures, Russian Academy of Sciences) was used.

D.A.T. contributed writing–conceptualization, writing, TEM investigations, and simulation; N.S.G. contributed sample preparation and characterization, and editing; Yu.V.P. contributed focused ion-beam modification, and review and editing; A.C. contributed TEM investigation, and review and editing; M.V.S. contributed conceptualization, simulation, and review and editing; and S.A.G. contributed project administration, conceptualization, and review and editing.

- [1] I. E. Dzyaloshinskii and B. A. Ivanov, Localized topological solitons in a ferromagnet, *JETP Lett.* **29**, 540 (1979).
- [2] A. S. Kovalev, A. M. Kosevich, and K. V. Maslov, Magnetic vortex-topological soliton in a ferromagnet with an easy-axis anisotropy, *JETP Lett.* **30**, 296 (1979).
- [3] S. Muhlbauer, B. Binz, F. Jonietz, C. Pfleiderer, A. Rosch, A. Neubauer, R. Georgii, and P. Boni, Skyrmion lattice in a chiral magnet, *Science* **323**, 915 (2009).
- [4] X. Z. Yu, Y. Onose, N. Kanazawa, J. H. Park, J. H. Han, Y. Matsui, N. Nagaosa, and Y. Tokura, Real-space observation of a two-dimensional skyrmion crystal, *Nature (London)* **465**, 901 (2010).
- [5] U. K. Rossler, N. Bogdanov, and C. Pleiderer, Spontaneous skyrmion ground states in magnetic metals, *Nature (London)* **442**, 797 (2006).
- [6] S. Heinze, K. von Bergmann, M. Menze, J. Brede, A. Kubetzka, R. Wiesendanger, G. Bihlmayer, and S. Blugel, Spontaneous atomic-scale magnetic skyrmion lattice in two dimensions, *Nat. Phys.* **7**, 713 (2011).
- [7] M. V. Dorokhin, A. V. Zdoroveyshchev, M. P. Temiryazeva *et al.*, Manipulation of micromagnetic structure of thin Co/Pt multilayer films by precise variation of Co and Pt thicknesses, *J. Alloys Compd.* **926**, 166956 (2022).
- [8] A. Fert, N. Reyren, and V. Cros, Magnetic skyrmions: Advances in physics and potential applications, *Nat. Rev. Mater.* **2**, 17031 (2017).
- [9] W. Jiang, G. Chen, K. Liu, J. Zang, S. G. teVelthuis, and A. Hoffmann, Skyrmions in magnetic multilayers, *Phys. Rep.* **704**, 1 (2017).
- [10] X. Chen, W. Kang, D. Zhu, X. Zhang, N. Lei, Y. Zhang, Y. Zhou, and W. Zhao, A compact skyrmionic leaky-integrate-fire spiking neuron device, *Nanoscale* **10**, 6139 (2018).
- [11] G. Chen, J. Zhu, A. Quesada, J. Li, A. T. N'Diaye, Y. Huo, T. P. Ma, Y. Chen, H. Y. Kwon, C. Won, Z. Q. Qiu, A. K. Schmid, and Y. Z. Wu, Novel chiral magnetic domain wall structure in Fe/Ni/Cu(001) films, *Phys. Rev. Lett.* **110**, 177204 (2013).
- [12] M. Benitez, A. Hrabec, A. Mihai, T. Moore, G. Burnell, D. McGrouther, C. Marrows, and S. McVitie, Magnetic microscopy and topological stability of homochiral Néel domain walls in a Pt/Co/AIO<sub>x</sub> trilayer, *Nat. Commun.* **6**, 8957 (2015).
- [13] S. D. Pollard, J. A. Garlow, J. Yu, Z. Wang, Y. Zhu, and H. Yang, Observation of stable Néel skyrmions in cobalt/palladium multilayers with Lorentz transmission electron microscopy, *Nat. Commun.* **8**, 14761 (2017).
- [14] J. A. Garlow, S. D. Pollard, M. Beleggia, T. Dutta, H. Yang, and Y. Zhu, Quantification of mixed Bloch-Néel topological spin textures stabilized by the Dzyaloshinskii-Moriya interaction in Co/Pd, *Phys. Rev. Lett.* **122**, 237201 (2019).
- [15] S. Woo, K. Litzius, B. Krüger, M.-Y. Im, L. Caretta, K. Richter, M. Mann, A. Krone, R. M. Reeve, M. Weigand, P. Agrawal, I. Lemesch, M.-A. Mawass, P. Fischer, M. Kläui, and G. S. D. Beach, Observation of room-temperature magnetic skyrmions and their current-driven dynamics in ultrathin metallic ferromagnets, *Nat. Mater.* **15**, 501 (2016).
- [16] L.-C. Peng, Y. Zhang, S.-L. Zuo, M. He, J.-W. Cai, S.-G. Wang, H.-X. Wei, J.-Q. Li, T.-Y. Zhao, and B.-G. Shen, Lorentz transmission electron microscopy studies on topological magnetic domains, *Chin. Phys. B* **27**, 066802 (2018).
- [17] C. Moreau-Lucaire, C. Moutafis, N. Reyren, J. Sampaio, C. A. F. Vaz, N. Van Horne, K. Bouzehouane, K. Garcia, C. Deranlot, P. Warnicke, P. Wohlhüter, J.-M. George, M. Weigand, J. Raabe, V. Cros, and A. Fert, Additive interfacial chiral interaction in multilayers for stabilization of small individual skyrmions at room temperature, *Nat. Nanotechnol.* **11**, 444 (2016).
- [18] S. McVitie, S. Hughes, K. Fallon, S. McFadzean, D. McGrouther, M. Krajnak, W. Legrand, D. Maccariello, S. Collin, K. Garcia, N. Reyren, V. Cros, A. Fert, K. Zeissler, and C. H. Marrows, A transmission electron microscope study of Néel skyrmion magnetic textures in multilayer thin film systems with large interfacial chiral interaction, *Sci. Rep.* **8**, 5703 (2018).
- [19] O. Boule, J. Vogel, H. Yang, S. Pizzini, D. De Souza Chaves, A. Locatelli, T. Mentès, A. Sala, L. Buda-Prejbeanu, O. Klein, M. Belmeguenai, Y. Roussigné, A. Stashkevich, S. MouradChérif, L. Aballe, M. Foerster, M. Chshiev, S. Auffret, I. Miron, and G. Gaudin, Room-temperature chiral magnetic skyrmions in ultrathin magnetic nanostructures, *Nat. Nanotechnol.* **11**, 449 (2016).
- [20] G. Chen, S. Pyo Kang, C. Ophus, A. T. N'Diaye, H. Young Kwon, R. T. Qiu, Ch. Won, K. Liu, Y. Wu, and A. K. Schmid, Out-of-plane chiral domain wall spin-structures in ultrathin in-plane magnets, *Nat. Commun.* **8**, 15302 (2017).
- [21] A. Samardak, A. Kolesnikov, M. Steblyi, L. Chebotkevich, A. Sadovnikov, S. Nikitov, A. Talapatra, J. Mohanty, and A. Ognev, Enhanced interfacial Dzyaloshinskii-Moriya interaction and isolated skyrmions in the inversion-symmetry-broken Ru/Co/W/Ru films, *Appl. Phys. Lett.* **112**, 192406 (2018).
- [22] W. Jiang, S. Zhang, X. Wang, C. Phatak, Q. Wang, W. Zhang, M. B. Jungfleisch, J. E. Pearson, Y. Liu, J. Zang, X. Cheng, A. Petford-Long, A. Hoffmann, and S. G. E. teVelthuis, Quantifying chiral exchange interaction for Néel-type skyrmions via Lorentz transmission electron microscopy, *Phys. Rev. B* **99**, 104402 (2019).
- [23] T. N. G. Meier, M. Kronseder, and C. H. Back, Domain-width model for perpendicularly magnetized systems with Dzyaloshinskii-Moriya interaction, *Phys. Rev. B* **96**, 144408 (2017).
- [24] S. L. Zhang, G. van der Laan, W. W. Wang, A. A. Haghighirad, and T. Hesjedal, Direct observation of twisted surface skyrmions in bulk crystals, *Phys. Rev. Lett.* **120**, 227202 (2018).
- [25] W. Legrand, N. Ronceray, N. Reyren, D. Maccariello, V. Cros, and A. Fert, Modeling the shape of axisymmetric skyrmions in magnetic multilayers, *Phys. Rev. Appl.* **10**, 064042 (2018).
- [26] K. Fallon, S. McVitie, W. Legrand, F. Ajejas, D. Maccariello, S. Collin, V. Cros, and N. Reyren, Quantitative imaging of hybrid chiral spin textures in magnetic multilayer systems by Lorentz microscopy, *Phys. Rev. B* **100**, 214431 (2019).
- [27] C. Chappert, H. Bernas, J. Ferre, V. Kottler, J.-P. Jamet, Y. Chen, E. Cambril, T. Devolder, F. Rousseaux, V. Mathet *et al.*, Planar patterned magnetic media obtained by ion irradiation, *Science* **280**, 1919 (1998).
- [28] D. A. Tatarskiy, N. S. Gusev, V. Yu. Mikhailovskii, Yu. V. Petrov, and S. A. Gusev, Control over the magnetic properties of Co/Pt-based multilayered periodical structures, *Tech. Phys.* **64**, 1584 (2019).
- [29] M. V. Sapozhnikov, S. N. Vdovichev, O. L. Ermolaeva, N. S. Gusev, A. A. Fraerman, S. A. Gusev, and Y. V. Petrov, Artificial dense lattice of magnetic bubbles, *Appl. Phys. Lett.* **109**, 042406 (2016).

- [30] K. Fallon, S. Hughes, K. Zeissler, W. Legrand, F. Ajejas, D. Maccariello, S. McFadzean, W. Smith, D. McGrouther, S. Collin, N. Reyren, V. Cros, Ch. H. Marrows, and S. McVitie, Controlled individual skyrmion nucleation at artificial defects formed by ion irradiation, *Small* **16**, 1907450 (2020).
- [31] S. Zhang, A. Petford-Long, and C. Phatak, Creation of artificial skyrmions and antiskyrmions by anisotropy engineering, *Sci. Rep.* **6**, 31248 (2016).
- [32] M. V. Sapozhnikov, N. S. Gusev, S. A. Gusev, D. A. Tatarskiy, Yu. V. Petrov, A. G. Temiryazev, and A. A. Fraerman, Direct observation of topological Hall effect in Co/Pt nanostructured films, *Phys. Rev. B* **103**, 054429 (2021).
- [33] M. V. Sapozhnikov, Y. V. Petrov, N. S. Gusev, A. G. Temiryazev, O. L. Ermolaeva, V. L. Mironov, and O. G. Udalov, Artificial dense lattices of magnetic skyrmions, *Materials* **13**, 99 (2020).
- [34] R. Heilbronner, The autocorrelation function: An image processing tool for fabric analysis, *Tectonophysics* **212**, 351 (1992).
- [35] B. Zang, K. Suzuki, and A. Liu, Estimation of volume-weighted average grain size in Fe-based nanocrystalline soft magnetic materials by autocorrelation function, *Mater. Charact.* **142**, 577 (2018).
- [36] L. Herrera Diez, M. Voto, A. Casiraghi, M. Belmeguenai, Y. Roussigné, G. Durin, A. Lamperti, R. Mantovan, V. Sluka, V. Jeudy, Y. T. Liu, A. Stashkevich, S. M. Chérif, J. Langer, B. Ocker, L. Lopez-Diaz, and D. Ravelosona, Enhancement of the Dzyaloshinskii-Moriya interaction and domain wall velocity through interface intermixing in Ta/CoFeB/MgO, *Phys. Rev. B* **99**, 054431 (2019).
- [37] I. L. Kalentyeva, O. V. Vikhrova, Yu. A. Danilov, A. V. Zdoroveyshchev, M. V. Dorokhin, Yu. A. Dudin, A. V. Kudrin, M. P. Temiryazeva, A. G. Temiryazev, S. A. Nikitov, and A. V. Sadovnikov, Effect of ion irradiation on the magnetic properties of CoPt films, *Phys. Solid State* **63**, 386 (2021).
- [38] N. S. Gusev, Yu. A. Dudin, A. V. Sadovnikov, and M. V. Sapozhnikov, Modification of the interfacial Dzyaloshinskii-Moriya interaction in cobalt/heavy metal films irradiated with helium ions, *Phys. Solid State* **63**, 1373 (2021).
- [39] M. V. Sapozhnikov, Skyrmion lattice in a magnetic film with spatially modulated material parameters, *J. Magn. Magn. Mater.* **396**, 338 (2015).
- [40] A. Vansteenkiste, J. Leliaert, M. Dvornik, M. Helsen, F. Garcia-Sanchez, and B. Van Waeyenberge, The design and verification of MuMax3, *AIP Adv.* **4**, 107133 (2014).
- [41] J. Leliaert, B. V. de Wiele, A. Vansteenkiste, L. Laurson, G. Durin, L. Dupre, and B. V. Waeyenberge, Current-driven domain wall mobility in polycrystalline permalloy nanowires: A numerical study, *J. Appl. Phys.* **115**, 233903 (2014).
- [42] M. V. Sapozhnikov, O. V. Ermolaeva, E. V. Skorokhodov, N. S. Gusev, and M. N. Drozdov, Magnetic skyrmions in thickness-modulated films, *JETP Lett.* **107**, 364 (2018).
- [43] D. A. Tatarskiy, “Fresnel contrast simulation for Gatan Microscopy Suite 3.4.1” (2020).
- [44] S. McVitie and M. Cushley, Quantitative Fresnel Lorentz microscopy and the transport of intensity equation, *Ultramicroscopy* **106**, 423 (2006).
- [45] S. McVitie and G. White, Imaging Amperian currents by Lorentz microscopy, *J. Phys. D: Appl. Phys.* **37**, 280 (2004).
- [46] H. Yang, A. Thiaville, S. Rohart, A. Fert, and M. Chshiev, Anatomy of Dzyaloshinskii-Moriya interaction at Co/Pt interfaces, *Phys. Rev. Lett.* **115**, 267210 (2015).
- [47] N. S. Gusev, A. V. Sadovnikov, S. A. Nikitov, M. V. Sapozhnikov, and O. G. Udalov, Manipulation of the Dzyaloshinskii-Moriya interaction in Co/Pt multilayers with strain, *Phys. Rev. Lett.* **124**, 157202 (2020).
- [48] A. N. Bogdanov and D. A. Yablonskiĭ, Thermodynamically stable “vortices” in magnetically ordered crystals. The mixed state of magnets, *JETP* **68**, 101 (1989).
- [49] See Supplemental Material at <http://link.aps.org/supplemental/10.1103/PhysRevB.110.064415> for additional micromagnetic and Fresnel contrast simulations of skyrmions and trivial vortices.